Jake A. Steiner
Design, Automation, Robotics, and Control (DARC) Lab,
Department of Mechanical Engineering and the Robotics Center,
University of Utah,
Salt Lake City, UT 84112
e-mail: Jake.Steiner@utah.edu

Lan N. Pham
Telerobotics Lab, Department of Mechanical Engineering and the Robotics Center,
University of Utah,
Salt Lake City, UT 84112
e-mail: Lan.Pham@utah.edu

Jake J. Abbott
Telerobotics Lab, Department of Mechanical Engineering and the Robotics Center,
University of Utah,
Salt Lake City, UT 84112
e-mail: jake.abbott@utah.edu

Kam K. Leang[1]
Design, Automation, Robotics, and Control (DARC) Lab,
Department of Mechanical Engineering and the Robotics Center,
University of Utah,
Salt Lake City, UT 84112
e-mail: kam.k.leang@utah.edu

Modeling and Analysis of a Soft Endoluminal Inchworm Robot Propelled by a Rotating Magnetic Dipole Field

In clinical practice, therapeutic and diagnostic endoluminal procedures of the human body often use a scope, catheter, or passive pill-shaped camera. Unfortunately, such devices used in the circulatory system and gastrointestinal tract are often uncomfortable, invasive, and require the patient to be sedated. With current technology, regions of the body are often inaccessible to the clinician. Herein, a magnetically actuated soft endoluminal inchworm robot that may extend clinicians' ability to reach further into the human body and practice new procedures is described, modeled, and analyzed. A detailed locomotion model is proposed that takes into account the elastic deformation of the robot and its interactions with the environment. The model is validated with in vitro and ex vivo (pig intestine) physical experiments and is shown to capture the robot's gait characteristics through a lumen. Utilizing dimensional analysis, the effects of the mechanical properties and design variables on the robot's motion are investigated further to advance the understanding of this endoluminal robot concept. [DOI: 10.1115/1.4053114]

Keywords: medical robotics, robot design, soft robots

1 Introduction

Procedures in the natural lumina of the human body are indispensable in minimally invasive diagnostic and therapeutic procedures [1]; however, complete controlled access to the entire gastrointestinal (GI) tract [2] and circulatory system [3] is challenging. A magnetically actuated soft inchworm robot concept recently presented in Ref. [4] can be exploited to produce controllable robotic therapeutic and diagnostic tools. As shown in Fig. 1, the robot consists of a deformable (soft) body between two magnets that are coaxially aligned with opposing polarity. A controllable rotating actuation magnet positioned outside of the patient, as illustrated in Fig. 1(*a*), induces a gait in the endoluminal robot that propels it through the lumen. The actuator magnet's axis of rotation and position need to be kept approximately perpendicular to the lumen and roughly above the robot, respectively. The separation distance of the actuator and robot significantly affects the gait. The image sequence in Fig. 1(*b*) portrays the induced gait, which is similar to that of an inchworm caterpillar's gait, shown for comparison in Fig. 1(*c*). First, there is an anchor-pull phase where the leading foot anchors and the lagging foot is pulled closer to the leading foot by contracting the body. This phase is followed by an anchor-push phase where the lagging foot is anchored and the leading foot is pushed forward by extending the body. Since the soft robot is mechanically simple, it can be adapted to various lumen sizes present in the body, and the external actuation magnet eliminates the need for complex mechanisms for locomotion within the robot. Although initial results show the potential for the robot to travel through the lumen, a thorough understanding of the physics and locomotion of the device is needed to develop and fully optimize the design. The focus of this paper is the modeling and analysis of the locomotion of the soft robot of Fig. 1. Dimensional analysis is then performed to efficiently study the effects of the various design variables on the robot's motion.

Endoluminal procedures in the GI tract traditionally involve pushing a long flexible scope from its proximal end [5,6]. In the early 2000s, passive capsule-shaped cameras were first used to inspect the bowels and reach regions traditional scope methods could not, such as the small intestine [7]. Capsule endoscopy relies on peristalsis, so only uncontrolled antegrade travel is possible. Since the motion and orientation are uncontrolled, the camera may fail to capture images of regions of interest [8]. In order to tackle the aforementioned deficiencies, endoscopic and capsule devices are becoming more robotic with the addition of controllable actuation. Controllable capsule-like robotic devices will enable orientation and position control [9], including retrograde travel (i.e., against peristalsis). This will expand clinicians' reach and capabilities during endoluminal procedures throughout the human body.

Many methods of endoluminal locomotion have been proposed, such as inchworm-like (anchor-pull and anchor-push) [10–13], legged [14–16], continuous track [17], worm screw [18–20], and vibration mechanisms [21]. The current challenge with endoluminal robots is creating a useful controllable device that can operate in a natural lumen for the duration of a procedure without damaging the lumen environment [22]. Battery-powered devices offer limited performance due to battery size, power requirements, and the time required for endoluminal procedures [23,24]. Inductive power has been proposed and is feasible in the GI tract. With limited power available (310 mW with a cylindrical power receiver 12-mm long and 10-mm diameter [25]), however, it may not be feasible to power both the locomotion and on-board instruments. Due to

[1]Corresponding author.

Contributed by the Mechanisms and Robotics Committee of ASME for publication in the Journal of Mechanisms and Robotics. Manuscript received April 12, 2021; final manuscript received November 12, 2021; published online February 18, 2022. Assoc. Editor: Guangbo Hao.

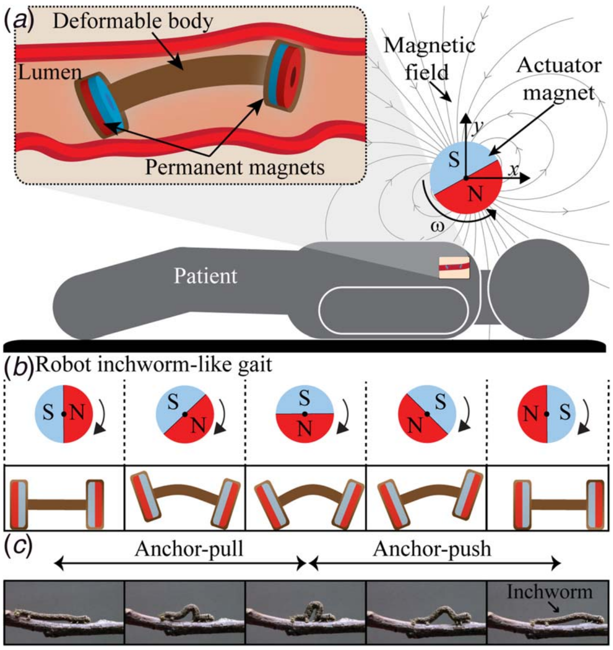

Fig. 1 The magnetically actuated soft inchworm robot has the potential to be used in endoluminal medical procedures across a variety of size scales. (*a*) Illustration of the potential use of the robot in a patient with an external rotating actuator magnet. (*b*) A sequence of images illustrating the gait induced in the robot by the rotation of the actuator magnet. The gait resembles that of an inchworm, having an anchor-pull and anchor-push phase. (c) Biological Inchworm gait for comparison. Photographs of inchworm by Mike E. Merchant, used with permission. Figure is not to scale.

the mechanical complexity, it would not be simple to scale the dimensions of the power receiver down to smaller sizes. On the other hand, magnetically actuated robots with permanent magnets benefit from scalability and can even be fabricated at the micrometer scale [26,27]. At this size, they could potentially operate in the human body's vasculature.

The soft inchworm robot concept illustrated in Fig. 1 has a simple design comprising only a soft (silicone) body and two magnets. Due to the simple structure, the device lends itself to scaling to various sizes to conform to diverse environments. For example, commercially available permanent magnets are widely available with dimensions as low as 1-mm in diameter. Alternatively, using additive manufacturing, work in Ref. [28] has shown that magnets with even smaller dimensions can be integrated directly into soft devices.

Establishing an understanding of the robot's mechanics of locomotion is essential to creating feasible and efficient endoluminal robotic devices that are optimized for their environment. The novelty of this work is the development of a new model for the gait of the magnetically driven inchworm robot. The model captures the robot's locomotion with a quasistatic approach by predicting the successive poses of the deformable device. Building on preliminary work [29], the model incorporates a more accurate geometrical and mechanical representation of the robot and its environment. Additionally, the model considers the effects of friction on the robot's feet and the deformation of the lumen. There are two main contributions of this work. The first is the development of an experimentally validated model with physical experiments. In comparison to experimental results (including the first demonstration of the robot traveling on an *ex vivo* intestine), the model accurately captures the robot's behavior through the environment. The model will provide insight to help guide the design process when customizing the robot for a specific environment. The second contribution is to elucidate the design variables' trends to better understand how to exploit the phenomena that create usable motion in the device. Using the validated model, dimensional analysis, via Buckingham Π theorem, is used to examine trends and scalability of the design.

The remainder of this paper is organized as follows. Section 2 describes the details of the model of the soft robot. Then, in Sec. 3, the model is validated with comparisons to experimental results in a rigid lumen and *ex vivo* pig intestine. Utilizing the validated model, Sec. 4 applies dimensional analysis to explore design trends and scalability. Section 5 discusses the results of the paper. Lastly, concluding thoughts are presented in Sec. 6.

2 Model

The soft endoluminal inchworm robot is driven by the magnetic interaction between the internal robot and an external actuator magnet located above the robot, as shown in Fig. 1. The robot moves due to alternating feet sticking and slipping as the robot's body deforms and the feet rotate. This behavior is created by the nonuniform magnetic actuation field, which causes asymmetric magnetic forces and torques on each foot of the symmetric robot.

To develop the model, first, the magnetic interactions that drive the system are briefly described. Second, a static model of the soft robot that captures the interactions with the environment is developed. Next, an iterative process is created to determine the robot's static equilibrium for a given actuator pose. Lastly, a discretized model is developed where the gait of the robot is determined by successive static equilibria and proper initial conditions.

2.1 Magnetic Actuation Model.

An external rotating magnetic field drives the soft robot in a lumen. For simplicity, it is assumed that all magnets in the model are perfect dipoles. This model is perfectly accurate for a uniformly magnetized sphere, and it is very accurate for an actual physical spherical magnet. For other shaped magnets (e.g., cubes, cylinders, rings), this model becomes increasingly accurate with greater distances [30]. The magnetic field $\boldsymbol{B}$ at a relative position $\boldsymbol{r}$ with respect to a dipole source $\boldsymbol{M}$ is defined as

$$\boldsymbol{B}(\boldsymbol{r}) = \frac{\mu_0}{4\pi}\frac{3(\boldsymbol{M}\cdot\hat{\boldsymbol{r}})\hat{\boldsymbol{r}} - \boldsymbol{M}}{\|\boldsymbol{r}\|^3} \quad (1)$$

where $\mu_0 = 4\pi\times 10^{-7}$ T m A^{-1} is the magnetic permeability of free space, $\hat{\boldsymbol{r}}$ is a unit vector in the direction of $\boldsymbol{r}$, and all vectors are described with respect to a common coordinate frame as depicted in Fig. 1(*a*) [31].

The gait of the robot is driven by the interaction of the magnets in the robot with the actuation magnet. All of the magnets in the system impose forces and torques on each other. The force $\boldsymbol{F}$ and torque $\boldsymbol{T}$ on a dipole $\boldsymbol{M}$ in a magnetic field $\boldsymbol{B}$ are given by

$$\boldsymbol{F} = (\boldsymbol{M}\cdot\nabla)\boldsymbol{B} \quad (2)$$

and

$$\boldsymbol{T} = \boldsymbol{M}\times\boldsymbol{B} \quad (3)$$

These induced forces and torques cause the body of the robot to elastically deform. This deformation, along with sticking and slipping of the contact points on the robot's feet, cause the robot to move in a deterministic direction within the lumen.

2.2 Locomotion Model.

Using the pairwise dipole–dipole interactions between all magnets in the system, the net magnetic force and torque on each of the robot's magnets can be calculated and used in a model describing the robot's deformation and movement through the environment. An accurate model will enable exploration of design variable trends (e.g., body length, dipole moments) and simulation of the robot's performance prior to physical realization.

By examining the physical robot in motion, it can be observed that the robot exhibits an inchworm-like gait (anchor-pull anchor-push) [29], as illustrated in Figs. 1(*b*) and 1(*c*). It has been found experimentally that the robot operates most predictably at low frequencies (typically 1–3 Hz) [4]. At this speed, during the entire gait cycle, at least one contact point between the environment and robot is not slipping. At these low frequencies, if the actuator magnet's rotation is stopped, the robot holds its position with minimal inertial effects. Due to these characteristics, a quasistatic modeling approach is used to capture the motion of the gait using classical beam theory and mechanics.

To model the quasistatic behavior of the robot, the actuator magnet's rotation is stepped through discretized angles (and positions if it is not fixed). At each time-step k, the actuator dipole angle θ is increased by an angle step ϕ, such that $\theta[k+1] = \theta[k] + \phi$. At each $\theta[k]$, an iteration process is used to find the static equilibrium of the robot. The robot's state of equilibrium is not unique and relies on boundary conditions based on the previous solution from time-step $k-1$.

This iterative process involves finding an error term ξ (described in Sec. 2.2.5), calculated for each iteration i. The ξ term is energy-like and gives insight into the off-equilibrium robot energy. A proportional-integral-derivative (PID) controller is used to drive the error term to zero, and thus the robot to a state of equilibrium, by changing the vertical boundary conditions of three points of the robot: the bottom of the two feet (η_A, η_B) and the body of the robot (η_C).

2.2.1 Model Setup. The robot and environment are assumed to be composed of cylindrical elements that are symmetric about the plane swept by the rotating actuator dipole. This allows the model to be simplified to two dimensions in the *x*/*y*-plane as shown in Fig. 2(*a*). Since the soft robot is reminiscent of an inchworm, the cylindrical ends are referred to as "feet" and the midsection as a "body." In the model, the feet are represented as rigid rectangles and the body as a deformable beam. The left foot is referred to as A with mass m_A, and the right foot is referred to as B with mass m_B. The body of the robot has mass m_{body}. Since the body's length is much longer than its thickness, classical beam theory is used to approximate the body deformation. It is also assumed that the feet remain perpendicular to the ends of the body. The lumen, which the soft robot is traveling in, is represented as a floor and a ceiling. The floor is a straight horizontal line at a distance $\mathscr{F}$ from the actuator magnet location. It is assumed that the robot's weight alone does not significantly deform the lumen it is in. In the case where the magnetic forces or torques are causing the robot to make contact with both the floor and ceiling surfaces, the lumen is allowed to deform. In the model, the ceiling can deform, whereas in real life, it is expected that the ceiling and floor would deform at approximately half of what the model predicts for ceiling deformation. The main difference here being the vertical displacement of the robot, but not the gait behavior itself. The undeformed location of the ceiling $\mathscr{C}$ is one-lumen diameter d_e above $\mathscr{F}$. Each possible point of contact—foot A, foot B, and the body—with the ceiling is modeled as an independent linear spring with stiffness k_e. Each point of contact with the ceiling and floor is able to make and break contact as the robot deforms and moves.

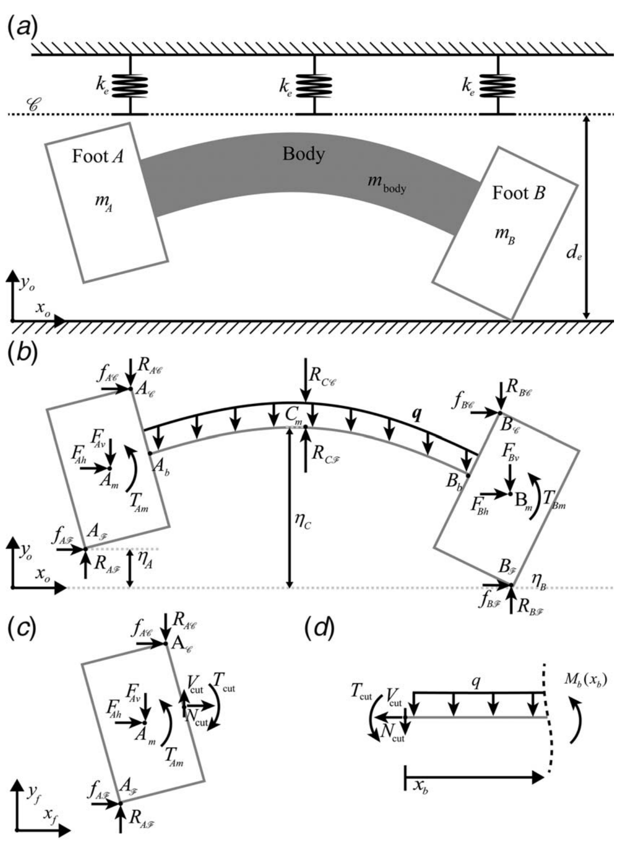

Fig. 2 Two-dimensional representation of the soft robot and lumen environment. (*a*) Mechanical system model. (*b*) Free body diagram of the robot. (*c*) Free body diagram of foot *A*. (*d*) Free body diagram of the body, cut at an arbitrary location.

A free body diagram of the soft robot is shown in Fig. 2(*b*). All force vectors are decomposed into their x_o and y_o components and torque is along the z_o axis. To represent a single dimension of a point, the subscript ends in x, y, or z. The world frame of the model is represented by a subscript o. The lumen–environment axis is along the x_o axis. Forces and torques on the feet act at the center of gravity of the foot (A_m and B_m). There is a vertical force (along y_o), horizontal force (along x_o), and a torque (along z_o) acting at the center of gravity for each foot. The vertical forces, F_{Av} and F_{Bv}, combine the weight of the foot with the vertical magnetic forces. The horizontal forces, F_{Ah} and F_{Bh}, are the horizontal components of the magnetic forces. The torques, T_{Am} and T_{Bm}, are the combined magnetic torques. The weight of the robot's body section is represented as a constant distributed load q.

Each segment of the robot has two possible reaction forces: one with the ceiling and one with the floor. The ceiling contact points, $A_{\mathscr{C}}$ and $B_{\mathscr{C}}$, are taken as the highest corners of the foot, and the floor contact points, $A_{\mathscr{F}}$ and $B_{\mathscr{F}}$, are the lowest corners. Each foot contact location has a reaction force R and friction f. For simplification, it is assumed that the reaction forces act at the center of gravity of the robot body, C_m. The body is also assumed frictionless since the friction at the feet dominates the inchworm gait.

The three ceiling reaction forces act independently. Without loss of generality, the reaction force between the ceiling and foot A is

$$R_{A\mathscr{C}} = \begin{cases} 0 & \text{if } A_{\mathscr{C}y} < \mathscr{C} \\ \epsilon_A k_e & \text{otherwise} \end{cases} \tag{4}$$

where $\epsilon_A = A_{\mathscr{C}y} - \mathscr{C}$ is the displacement of the spring defined for foot A. The reaction forces with the floor are found using the equilibrium equations described in Sec. 2.2.2.

For each iteration at time-step k, it is assumed that one contact point on one foot is fixed in the x_o direction from the prior time-step $k-1$, and friction forces are computed for the non-fixed contact points. The friction force between the foot and the ceiling is

$$f_{A\mathscr{C}} = \delta_{A\mathscr{C}} \mu_s R_{A\mathscr{C}} \tag{5}$$

where μ_s is the static friction coefficient, and $\delta_{A\mathscr{C}} \in [-1, 1]$ encodes the direction and proportion of static friction used. For each iteration i and for each of the non-fixed contact points, the δ term is updated based on if a contact point has moved in the $+x_o$ or $-x_o$ direction relative to the prior time-step $k-1$. The update equation for δ with respect to $A_{\mathscr{C}}$ is

$$\delta_{A\mathscr{C},i+1} = \begin{cases} \delta_{A\mathscr{C},i} + \Delta & \text{if } A_{\mathscr{C}x,i} < A_{\mathscr{C}x}[k-1] \\ \delta_{A\mathscr{C},i} - \Delta & \text{if } A_{\mathscr{C}x,i} > A_{\mathscr{C}x}[k-1] \\ \delta_{A\mathscr{C},i} & \text{otherwise} \end{cases} \tag{6}$$

where Δ is a tuning gain that determines the amount δ can change in each iteration. The point $A_{\mathscr{C},i}$ is found at the end of each iteration i when the robot placement in the environment is determined (Sec. 2.2.4). The point $A_{\mathscr{C}}[k]$ is the final value of $A_{\mathscr{C},i}$ at time-step k. To smooth the friction values and reduce jittering of the solution, an infinite impulse response filter is used on all non-fixed contact point friction forces. The friction force at the fixed contact point is found using the equilibrium equations shown next.

2.2.2 Equilibrium Equations. The equilibrium equations used to solve for the unknown forces at each iteration i are described. First, during each iteration, the forces and torques from the dipole–dipole interactions are calculated based on the new positions of the magnets using the following equilibrium equations (refer to free body diagram shown in Fig. 2(*b*)):

$$\sum F_x = f_{A\mathscr{C}} + f_{B\mathscr{C}} + f_{A\mathscr{F}} + f_{B\mathscr{F}} + F_{Ah} + F_{Bh} = 0 \tag{7}$$

$$\sum F_y = -R_{A\mathscr{C}} - R_{B\mathscr{C}} - R_{C\mathscr{C}} + R_{A\mathscr{F}} + R_{B\mathscr{F}} + R_{C\mathscr{F}} - F_{Av} - F_{Bv} - ql_b = 0 \tag{8}$$

$$\begin{aligned}\sum M_{A_m} = {} & (A_{\mathscr{F}x} - A_{mx})R_{A\mathscr{F}} + (A_{my} - A_{\mathscr{F}y})f_{A\mathscr{F}} \\ & + (A_{mx} - A_{\mathscr{C}x})R_{A\mathscr{C}} + (A_{my} - A_{\mathscr{C}y})f_{A\mathscr{C}} \\ & + (B_{\mathscr{F}x} - A_{mx})R_{B\mathscr{F}} + (A_{my} - B_{\mathscr{F}y})f_{B\mathscr{F}} \\ & + (A_{mx} - B_{\mathscr{C}x})R_{B\mathscr{C}} + (A_{my} - B_{\mathscr{C}y})f_{B\mathscr{C}} \\ & + (A_{mx} - B_{mx})F_{Bv} + (A_{my} - B_{my})F_{Bh} \\ & + (C_{mx} - A_{mx})(R_{C\mathscr{F}} - R_{C\mathscr{C}}) \\ & + (A_{mx} - (A_{bx} + B_{bx})/2)ql_b + T_{Am} + T_{Bm} = 0\end{aligned} \tag{9}$$

along with the displacement boundary conditions, the reaction forces $R_{A\mathscr{F}}$, $R_{B\mathscr{F}}$, and $R_{C\mathscr{F}}$, and the friction force of the fixed point can be found.

2.2.3 Robot Deformation. The body of the robot is assumed to be homogeneous and elastic. The deflection is found by solving

$$\frac{d^2}{dx_b^2}\mathcal{B}_y = \frac{M_b(x_b)}{EI} \tag{10}$$

where $M_b(x_b)$ is the moment along the body, $\mathcal{B}_y$ is the vertical offset of each discretized point along the centerline of the body beam, E is Young's modulus, and I is the second moment of area of the body. To determine $M_b(x_b)$, a "cut" is made where the beam connects to the foot at point A_b for foot A (shown in Figs. 2(*c*) and 2(*d*)). The torque T_{cut} and forces V_{cut} and N_{cut} on the ends of the body can be found by

$$\begin{aligned}T_{cut} = {} & (A_{bx} - A_{\mathscr{C}x})R_{A\mathscr{C}} + (A_{by} - A_{\mathscr{C}y})f_{A\mathscr{C}} \\ & + (A_{\mathscr{F}x} - A_{bx})R_{A\mathscr{F}} + (A_{by} - A_{\mathscr{F}y})f_{A\mathscr{F}} \\ & + (A_{bx} - A_{mx})F_{Av} + (A_{by} - A_{my})F_{Ah} + T_{Am}\end{aligned} \tag{11}$$

$$V_{cut} = R_{A\mathscr{C}} - R_{A\mathscr{F}} + F_{Av} \tag{12}$$

and

$$N_{cut} = -f_{A\mathscr{F}} - f_{A\mathscr{C}} - F_{Ah} \tag{13}$$

The moment along the beam can now be found using (Fig. 2(*d*))

$$M_b(x_b) = -1/2qx_b^2 - V_{cut}x_b - T_{cut} \tag{14}$$

Plugging the above expression into Eq. (10), the following result is obtained:

$$\mathcal{B}_y = (-1/24qx_b^4 - 1/6V_{cut}x_b^3 - 1/2T_{cut}x_b^2 + c_1x + c_2)/(EI) \tag{15}$$

where the boundary conditions η_A and η_B can be used to solve for the constants of integration c_1 and c_2.

2.2.4 Robot Placement in Environment. Once the body deformation is found at the end of the ith iteration, the robot's location in the environment can be determined. First, the feet are added perpendicular to the body. Then, the robot's location in the world frame is found based on which reaction force is larger. The foot corner location with the highest reaction force is kept fixed in the x_o displacement from the same corner in the previous time-step. The vertical offset of each foot is determined by η_A and η_B. Due to the unknown amount of foot rotation between iteration i and $i+1$, only $\eta_{A,i}$ and $\eta_{B,i}$ can be fixed in the solution at ith iteration. The $\eta_{C,i}$ term is only used as a boundary condition when determining body deflection.

2.2.5 Error Term. The error term, ξ, is an energy-like function that gives insight into the off-equilibrium energy of the robot. To find the equilibrium, the inputs to the model are the displacements η_A, η_B, and η_C. The $\eta_{A,i}$ and $\eta_{B,i}$ terms are used to define the vertical offsets of foot A and B during the ith iteration. The $\eta_{C,i}$ term is used as a boundary condition to solve for the over constrained beam deflection of the body. The error term ξ and input term η have different equations for the feet and body of the robot due to the different mechanics of the sections.

For feet A and B, the inputs $\eta_{A,i+1}$ and $\eta_{B,i+1}$ are found using the following PID update law (shown for foot A and is analogous for foot B):

$$\eta_{A,i+1} = k_P(\xi_{A,i}) + k_D(\xi_{A,i-1} - \xi_{A,i}) + k_I\sum_{i=0}^{i}\xi_{A,i} \tag{16}$$

where k_P, k_D, and k_I are constants, and $\eta_A, \eta_B \in [0, \infty)$. For the body, instead of an integral term, the y_o position at the center of the beam is used ($C_{my,i}$), hence

$$\eta_{C,i+1} = k_P(\xi_{C,i}) + k_D(\xi_{C,i-1} - \xi_{C,i}) + C_{my,i} \tag{17}$$

At equilibrium, the error term ξ is zero. The error term is based on the assumption that for the robot to be in static equilibrium, the following statement is true for each section (foot A, foot B, and body) of the robot: (1) the section's reaction force with the floor is zero or (2) the section's reaction force with the floor is positive and the section is touching the floor. The equations work to drive the robot to satisfy the assumption by independently changing the height of each foot and the midpoint of the body based on the reaction forces solved for in Eqs. (7) through (9).

The error term for the two feet of the robot, ξ_A and ξ_B, is found with the multiplication of a term related to distance and a term related to force, α and β, respectively. The assumption above has two conditions that are both represented in the error function by α and β. Condition (1) is based on direction and displacement, which is captured with the α term. The other is based on the reaction force, which is captured with β. The error equation (shown for A and is analogous for B and C) is given by

$$\xi_{A,i} = \alpha_{A,i}\beta_{A,i} \tag{18}$$

The β term is related to the magnitude of the floor reaction force (shown for A and in analogous for B and C):

$$\beta_{A,i} = 1 - \frac{F_n - |\mathrm{sat}(R_{A\mathscr{F}} \pm F_n)|}{F_n} \tag{19}$$

where F_n is a parameter to normalize β. This term needs to be tuned depending on the magnitude of the forces in the model. The $\beta \in [0, 1]$ term dictates how much influence the force has on the ξ term. If the force is large, then $\beta = 1$ and if the force is zero, then $\beta = 0$.

The α term relates to condition (2) and determines the direction the distance η needs to change such that the boundary conditions for the ceiling and floor are met: reaction forces should be positive and if there is a positive reaction force, there needs to be contact there. The α term for the feet is (shown with foot A and is analogous for foot B) given by

$$\alpha_{A,i} = \begin{cases} (\mathscr{F} - A_{\mathscr{F}y})k_1 & \text{if } R_{A\mathscr{F}} > 0 \\ (\mathscr{C} - A_{\mathscr{C}y})k_1 & \text{if } R_{A\mathscr{F}} < 0 \ \& \ A_{\mathscr{C}y} < \mathscr{C} \\ \frac{-k_e\epsilon_A - R_{Af}}{k_e} k_2 & \text{if } R_{A\mathscr{F}} < 0 \ \& \ A_{\mathscr{C}y} > \mathscr{C} \\ 0 & \text{otherwise} \end{cases} \tag{20}$$

where the k_1 and k_2 terms are used to scale the influence on ξ. In the above equation, there are three cases where α is nonzero, explained below with respect to foot A, but foot B is found in an analogous manner:

(1) If the reaction force with the floor $R_{A\mathscr{F}}$ is positive, then α_A is based on the distance from the bottom of the foot $A_{\mathscr{F}y}$ to the floor $\mathscr{F}$.
(2) If the reaction force with the floor $R_{A\mathscr{F}}$ is negative and the foot is not touching the ceiling, then α_A is based on the distance from the top of the foot $A_{\mathscr{C}}$ to the nominal ceiling $\mathscr{C}$.
(3) If the reaction force with the floor $R_{A\mathscr{F}}$ is negative and the foot is already touching the ceiling, then α_A is based on how much the spring displacement ϵ_A would need to increase to balance out the reaction force with the floor.

Next, the error term for the body is explained. The α term for the midsection is defined differently than the feet. This is due to the system being very responsive to changes in this boundary condition. It was found that the following definition worked well:

$$\alpha_{C,i} = \begin{cases} k_3 & \text{if } R_{Cf} > 0 \text{ and } \min(\mathcal{B}_y) - \frac{d_b}{2} < \mathscr{F} \\ -k_3 & \text{if } R_{Cf} > 0 \text{ and } \min(\mathcal{B}_y) - \frac{d_b}{2} > \mathscr{F} \\ \frac{-k_C\epsilon_C - R_C}{k_C} k_4 & \text{if } R_{Cf} < 0 \text{ and } \max(\mathcal{B}_y) + \frac{d_b}{2} > \mathscr{C} + \epsilon_c \\ k_3 & \text{if } R_{Cf} < 0 \\ 0 & \text{otherwise} \end{cases} \tag{21}$$

where $\min(\mathcal{B}_y)$ and $\max(\mathcal{B}_y)$ are the lowest and highest points on the centerline of the body $\mathcal{B}_y$, respectively, k_C is the spring constant of the ceiling, and k_3 and k_4 are gains that can be adjusted. It is noted that in many scenarios, the robot body does not contact the environment during travel. If this is the case, for simplicity the η_c and $R_{C\mathscr{F}}$ terms could be neglected in the model.

2.2.6 Convergence. The output of the model converges when the deformation of the beam is sufficiently low between iterations, that is

$$\mathcal{E} = \text{norm}(\mathcal{B}_{y,i+1} - \mathcal{B}_{y,i}) \tag{22}$$

Once $\mathcal{E}$ is below threshold $\mathcal{E}_{\text{conv}}$, the static model has converged and the time increments to $k+1$. In some cases, the model oscillates between two different equilibrium points and a maximum number of iterations $i_{\max}$ is set for this case.

3 Model Validation

An experimental setup was created to compare the model predictions to physical experimental results. The experimental setup is

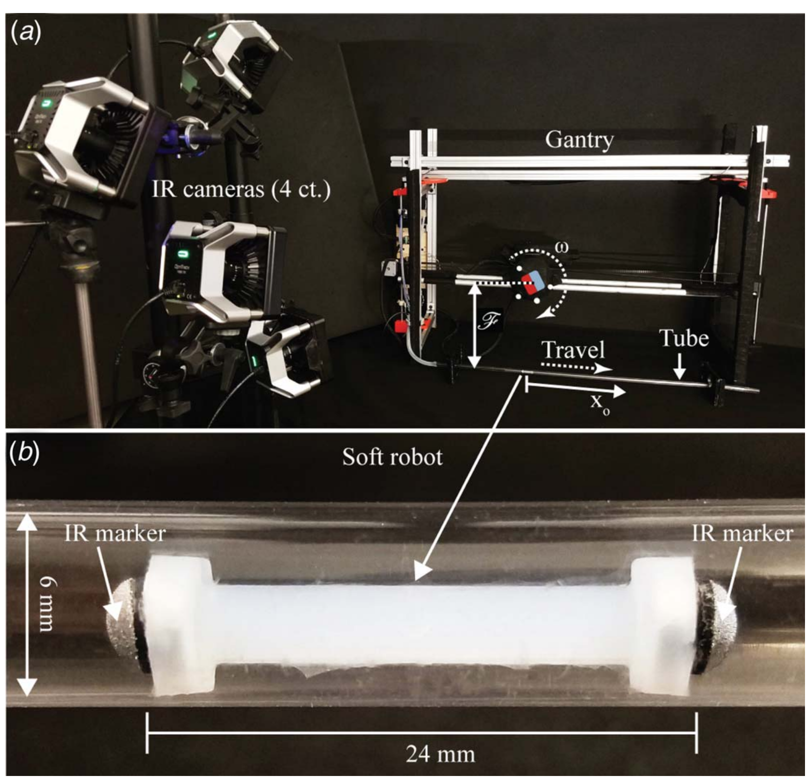

Fig. 3 The experimental setup used to test the robot. (*a*) Overall setup showing gantry, IR cameras, rotating magnet, lumen, and soft robot. (*b*) Detailed view of the soft robot in plastic lumen with IR markers on each end.

shown in Fig. 3(*a*). To validate the model, two environments are tested. First, the model output is compared to the robot in a rigid 6-mm diameter polycarbonate tube. Second, the model is compared to the robot actuated on an *ex vivo* pig intestine. The actuator magnet used has a dipole strength, M_a, of 205 A m^2 (K&J Magnetics, DZ0X8-N52). The height of the actuator magnet above the robot can be adjusted. In each trial, the robot starts directly underneath the actuator magnet at $x_o = 0$, then the actuator magnet was rotated clockwise, causing the robot to propel itself in the $+x$ direction. An infrared (IR) motion-capture system was used to track the position of the robot. Two IR markers, one on each foot, were added to the robot to enable tracking, as shown in Fig. 3(*b*). The soft robots used in both experimental setups were fabricated with a vacuum injection silicone mold. The modulus of elasticity was experimentally determined by securing the robot as a horizontal cantilever beam and measuring the deflection when a small weight was added. The modulus of elasticity of the body was found to be 1370 kPa. The magnets in the feet each have a dipole moment of 0.011 A m^2 (1.17×10^6 A/m, K&J R211-N52).

In the polycarbonate lumen, the model predictions are compared to experimental results for four different configurations. The soft robot used has feet with a diameter of 5 mm and a length of 2.2 mm. The length of the body section is 20 mm, and the body diameter is 2.5 mm. The tube is filled with water to better represent a biological lumen. The static friction coefficient between the silicone robot and lumen is experimentally determined to be 0.75. To approximate the interaction between the silicone feet and effectively rigid lumen environment, the environment spring stiffness was set to 80 N/m. The rest of the design parameters are aligned with the nominal design described in Table 1. The experiments are conducted at four different separation distances between the actuator magnet's axis of rotation and floor of the lumen, $\mathscr{F}$: 23 cm, 25 cm, 27 cm, and 29 cm. At each $\mathscr{F}$, 30 trials are performed where the robot is driven from $x = 0$ to 100 mm. The results are shown in Fig. 4. The raw position data from the IR camera motion-capture system are downsampled to 1 Hz (one measurement per gait cycle) and the velocity of the robot is calculated with central difference differentiation. The velocity data of the 30 trials are binned for each 1 mm of travel along the x_o axis. The solid black line is the average velocity of the physical robot over 30 trials. The gray shaded areas are ± 1 standard deviation around the average velocity of the physical robot. To determine the model simulation velocity, the position data are downsampled to 1 Hz, and the robot's velocity is calculated with central difference differentiation. The dashed line is the model results for the velocity of the robot. Overall, the developed model captures the changing velocity profile of the gait of the soft robot as it travels away from the actuator magnet at four different experimental setups in this rigid lumen.

Next, model predictions are compared to an *ex vivo* pig intestine environment, adding additional compliance under the feet of the robot. The test environment is shown in Fig. 5(*a*). The pig's small intestine is cut along the length and laid over a half-cylindrical trough (to enable visualization/localization), which is submerged in water. The friction coefficient is experimentally determined to be 2.7. The soft robot used has feet with a diameter of 5 mm and a length of 2 mm. The length of the body section is 20 mm, and the body diameter is 2 mm. The separation distance between the actuator magnet's axis of rotation and floor, $\mathscr{F}$, is 200 mm. The rest of the properties are the same as in the prior experiment. The robot starts directly underneath the actuator magnet ($x = 0$) and is driven in the $+x$ direction 80 mm (Fig. 5(*b*)). The test was run 60 times, and the results are shown in Fig. 5(*c*); the model prediction is shown with a dashed line. The lumen diameter and ceiling properties are not used for this model because the modeled environment is a trough.

4 Impact on Design

The experimentally validated model is now used to explore the influence of the various design parameters on the robot's performance. Prior work has not explored design trends and performance. For example, in Ref. [4], the forces and torques on a robot during the gait are shown in detail; however, the effects of parameters on performance is not known. A target environment will likely impose constraints on specific parameters, such as actuator magnet minimum separation from the robot or material of the soft robot. To support optimization of the robot for an environment, an understanding of the design trends is crucial.

4.1 Dimensional Analysis. The step size S per revolution of the actuator magnet is chosen as the dependent output variable.

Table 1 The chosen repeating variables, nonrepeating variables, and dimensionless Π groups of the modeled system

Repeating variables	Symbol	Units		Nominal design
Env. lumen diameter	d_e	m		6.0e-3
Env. ceiling stiffness	k_e	kg/s^2		8.0e1
Acceleration of gravity	g	m/s^2		9.81
Env. magnetic permeability	μ_e	kg m/(s^2 A^2)		$4\pi \times 10^7$
Nonrepeating variables	**Symbol**	**Units**	**Π group**	**Nominal design**
Step size	S	m	$\Pi_0 = S/d_e$	–
Env. static friction	η_s		$\Pi_1 = \eta_s$	7.5×10^{-1}
Actuator to floor distance	$\mathscr{F}$	m	$\Pi_2 = \mathscr{F}/d_e$	2.5×10^{-1}
Actuator dipole moment	M_a	A m^2	$\Pi_3 = M_a{}^2\mu_e/(d_e^5 k_e)$	2.05×10^2
Robot body length	l_b	m	$\Pi_4 = l_b/d_e$	1.0×10^{-2}
Robot foot length	l_f	m	$\Pi_5 = l_f/d_e$	2.0×10^{-3}
Robot body diameter	d_b	m	$\Pi_6 = d_b/d_e$	2.5×10^{-3}
Robot central-lumen diameter	d_l	m	$\Pi_7 = d_l/d_e$	0
Robot foot diameter	d_f	m	$\Pi_8 = d_f/d_e$	5.0×10^{-3}
Robot silicone density	ρ_s	kg/m^3	$\Pi_9 = \rho_s g d_e^2/k_e$	2.06×10^3
Robot modulus of elasticity	E	kg/(m s^2)	$\Pi_{10} = E\, d_e/k_e$	5.93×10^5
Robot magnetization	Ψ_m	A/m	$\Pi_{11} = \Psi_m^2 \mu_e d_e/k_e$	1.17×10^6
Robot magnet/foot vol. frac.	V_m		$\Pi_{12} = V_m$	2.40×10^1
Robot magnet density	ρ_m	kg/m^3	$\Pi_{13} = \rho_m d_e^2\, g/k_e$	5.26×10^3
Robot dipole angle, foot *A*	θ_{MA}		$\Pi_{14} = \theta_{MA}$	π
Robot dipole angle, foot *B*	θ_{MB}		$\Pi_{15} = \theta_{MB}$	0

Note: The last column shows the parameter values of the nominal design used throughout for comparison of design trends. In the following figures, the nominal design is marked with a black star.

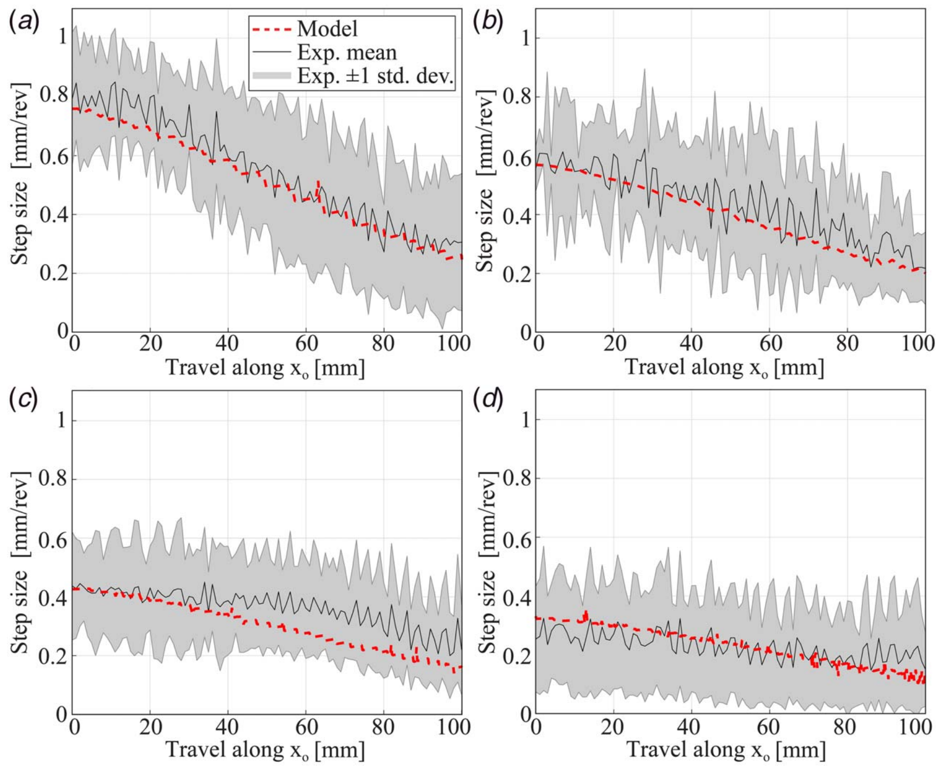

Fig. 4 Results of experimental verification of the model. The distance from the actuator magnet's axis of rotation and the floor of the tube is (*a*) 23 cm, (*b*) 25 cm, (*c*) 27 cm, and (*d*) 29 cm. Each plot comprises 30 experimental trials. The solid line is the average step size of the physical robot over those trials, and the shaded area shows ± 1 standard deviation.

The velocity v is related to step size S by $v = S\omega$, where ω is the angular velocity of the actuator magnet in hertz. There are three main types of independent variables: environment variables, actuator magnet variables, and soft robot variables (Fig. 6). The environment variables include the diameter of the lumen d_e, the lumen ceiling stiffness k_e, the acceleration of gravity g, the magnetic permeability of the environment μ_e (which in practice will typically be the permeability of free space μ_0), and the static friction of the robot with the environment η_s. Of these environmental variables, the system designer can only influence the static friction between the soft robot and the lumen environment (through a choice of material and surface property). The actuator magnet variables are fairly limited, comprising the distance from the dipole axis of rotation to the floor $\mathscr{F}$ and the strength of the actuator dipole moment M_a (note that, since the quasistatic step size of the soft robot is modeled, the angular velocity of the actuator magnet is not included as a relevant independent variable). Finally, the variables relating to the soft robot are numerous, including body length l_b, foot length l_f, body diameter d_b, central-lumen diameter d_l, foot diameter d_f, soft-material density ρ_s, foot magnet volume fraction (the fraction of the foot volume that is composed of the embedded magnet) V_m, density of magnet ρ_m, body modulus of elasticity E, magnetic field strength Ψ_m, dipole angle θ_{MA} for foot A, and dipole angle θ_{MB} for foot B.

With a total of 19 variables that describe the system (18 independent variables plus the output variable), comprising four primary dimensions (kg, m, s, and A), the Buckingham Π theorem [32] states that the physics of the system can be fully described by $19 - 4 = 15$ dimensionless Π groups (i.e., 14 independent dimensionless variables plus the resulting dimensionless output variable). Four linearly independent variables each containing at least one of the four primary dimensions are chosen to be used throughout the nondimensionalization process. This set of four variables, called repeating variables, are used to create the nondimensional Π groups. For the system described, four environmental variables

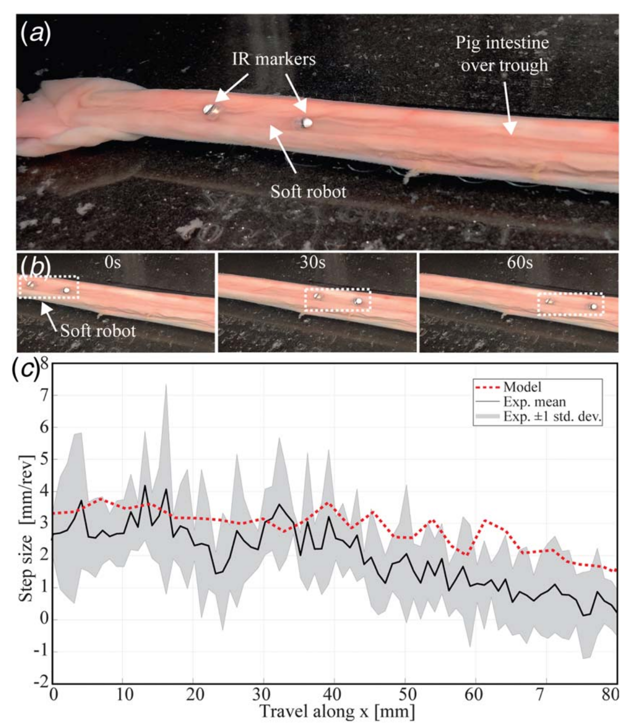

Fig. 5 Test environment and comparison to model predictions using an *ex vivo* pig intestine. (*a*) The pig intestine is cut along the length and laid over a half-cylindrical trough. (*b*) Time-lapse of the robot traveling through the environment. (*c*) The average velocity of 60 experimental trials is shown with a solid line, and the shaded area shows ± 1 standard deviation. The model prediction is shown with a dashed line.

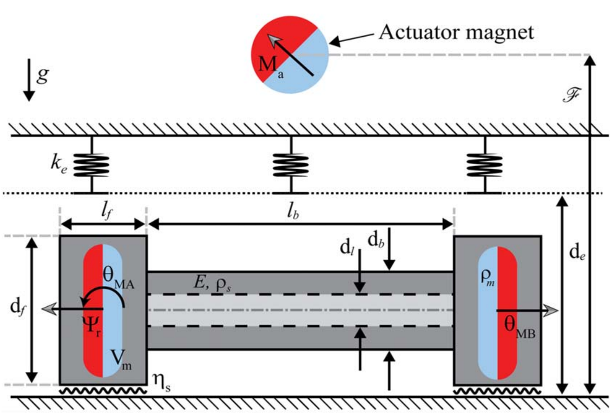

Fig. 6 Dimensions and variables used in the modeled system

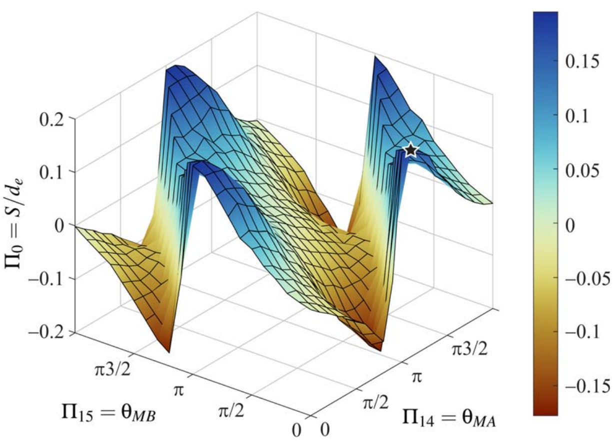

Fig. 7 Robot output trends with different combinations of dipole moment angles in foot *A* (θ_{MA}) and foot *B* (θ_{MB}). The nominal design (parameters shown in Table 1) is marked with a black star.

outside of the system designer's control create a suitable set of repeating variables: d_e for m, g for s, k_e for kg, and μ_e for A. After this choice, the resulting Π groups are constructed deterministically and are shown in Table 1. This proposed nondimensionalization, although not unique, seems to be a good choice for guiding future system designs for a given application area (i.e., set of lumen properties).

4.2 Justifying the Original Concept. In all of the prior work relating to the soft robot concept which is the focus of this work [4,29], only coaxial parallel and coaxial antiparallel arrangements of the magnetic dipoles embedded in the robot's feet have been investigated. It was experimentally determined in Ref. [4] that coaxial antiparallel dipole moments produce more robot motion along the lumen than coaxial parallel dipole moments. However, it is not known if there are potential benefits to magnetizing the robot's magnets in a different way, so here the coaxial antiparallel arrangement is briefly explored to see if it is truly optimal. Using the model created, all combinations of θ_{MA} and θ_{MB} with a resolution of 0.314 rad (18 deg) are simulated to determine the effect of the arrangement on the step size. The results are shown in Fig. 7. It is found that the maximum step size occurs at $[\theta_{MA}, \theta_{MB}] \in \{[0, \pi], [\pi, 0], [2\pi, \pi], [\pi, 2\pi]\}$, which are all coaxial parallel arrangements, justifying the original soft robot concept. For the rest of the simulations in this paper, the dipole angles will be kept at $[\theta_{MA}, \theta_{MB}] = [\pi, 0]$.

4.3 Design Trends. From the above result, it is concluded that there is no need to consider Π_{14} and Π_{15} further. This still leaves 13 independent variables that affect robot motion. Starting from the nominal design and varying only one independent parameter at a time, trends in (nondimensional) step size as a function of important Π groups are shown in Fig. 8. A few trends that are significant in optimizing robot performance can be observed. The robot's step size is primarily based on how much the robot can contract and expand the body along with the rotation of the feet. The effects of all the design variables on the robot motion can be roughly summarized into four categories:

(1) Variables that decrease the flexural stiffness of the robot's body lead to an increase in step size. Variables that affect flexural stiffness include: d_b, d_l, E, and l_b. The step size increases until the robot is too flexible to keep the feet from sticking together because of the magnets in the feet. Increasing l_b increases the step size up to a point at which the length no longer adds much additional rotation of the feet due to the body contacting the lumen. The effects of l_b and E can be seen in Π_4 and Π_{10} in Figs. 8(*c*) and 8(*e*).
(2) Variables that increase the magnetic forces and torques on a given robot cause an increase in step size. This can be done by increasing M_a, V_m, and Ψ_m (increasing Ψ_m is usually not possible as the highest grade of magnets is often already used) or decreasing $\mathscr{F}$. This trend is limited by the amount the robot can contract in the anchor-pull phase of the gait. Also, if the inter-magnetic forces between the actuator magnet and robot are too great, the robot will be pinned against the lumen wall, unable to move forward. The effects of M_a and V_m can be seen in Π_3 and Π_{12} in Figs. 8(*b*) and 8(*f*).
(3) Increasing forces that hinder the robot motion, such as ρ_s, ρ_m, and η_s, decrease the velocity. If the friction between the robot and lumen is too low, the robot will not be able to move. The effects of η_s and ρ_s can be seen in Π_1 and Π_9 in Figs. 8(*a*) and 8(*d*).
(4) Increasing d_f increases the step size the robot takes for a given foot rotation. Larger foot diameters lead to a more significant step with the same angle of rotation. This is, of course, limited by the environmental lumen diameter.

Of course, all these trends have limits and cannot be infinitely exploited. For example, if the modulus of elasticity of the body is continuously decreased (with the intent of causing the body to have greater deformation leading to a greater rotation of the feet and a larger step), at some point the body is not rigid enough to keep the two embedded magnets separated, and the feet of the robot will stick together.

4.4 Scaling. There are two intuitive ways to scale the robot to different lumen environments. The simplest way, which is referred to as the *naive method*, is to scale the robot's length dimensions linearly with the target lumen environment diameter while keeping all other properties constant. This method would be simple to achieve and would not require changing the material properties of the robot. The second method is to use the Π groups from Table 1 to scale the robot design nondimensionally by keeping Π_1 through Π_{15} constant. Both methods are investigated using the model. The robot's nominal design, with an environment lumen diameter d_e of 6 mm, is scaled up to 12 mm (2×) and down to 0.06 mm (0.01×). Forty logarithmically spaced scales are modeled, and the performance for the two methods is compared in Fig. 9.

Using the naive scaling method, the output is not predictable without a model and will not necessarily follow similar trends if a different initial design is used. Scaling d_e up to two times the nominal value of 6 mm, the robot output Π_0 decreases and the velocity increases. A decrease in Π_0 as lumen diameter increases means the velocity increased at a slower rate than lumen diameter. As the nominal d_e is scaled down to about 0.6 mm (0.1×), Π_0 decreases 85%. From a scale factor of 0.1–0.03, there is a slight increase and decrease in Π_0. This is due to the timing of the

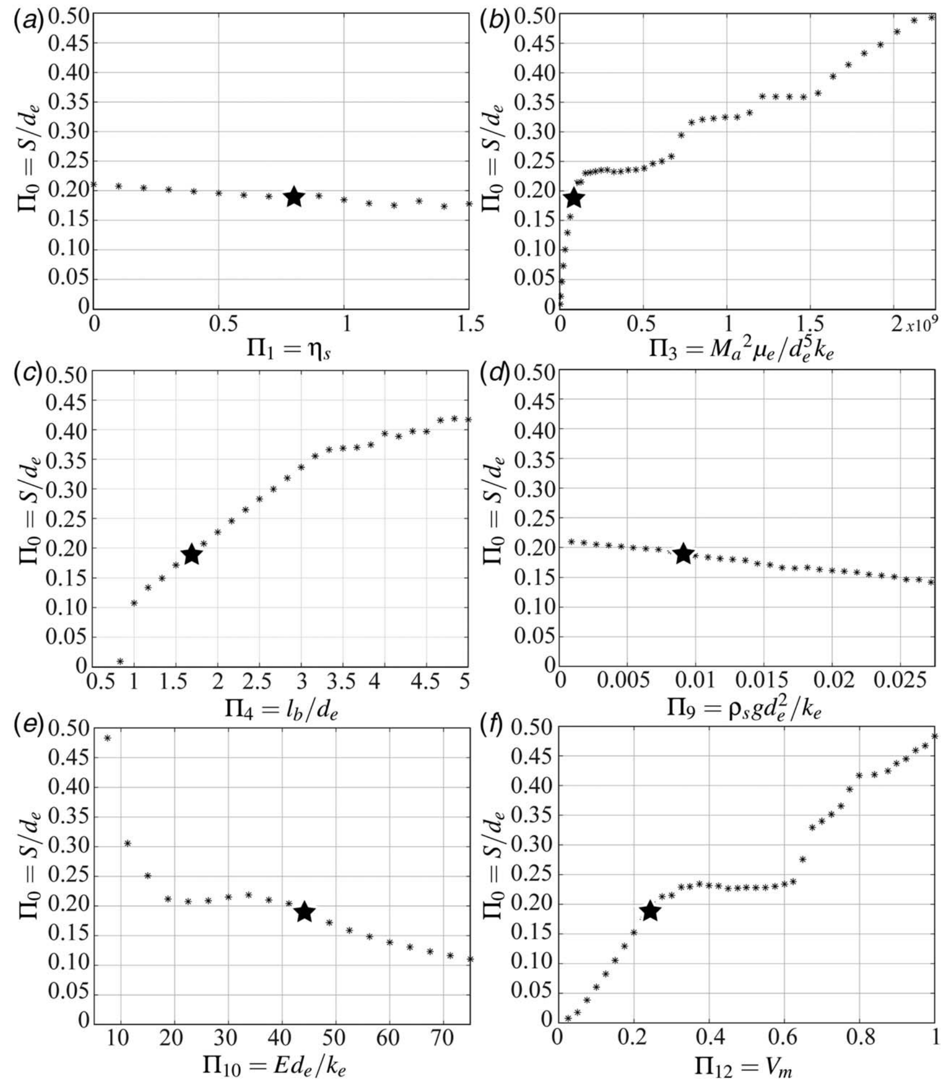

Fig. 8 Dimensionless trends for six Π groups of the modeled soft robot. Each plot shows the value of $\Pi_0 = S/d_e$ as a single independent Π group is changed relative to a nominal design (indicated with a black star).

inchworm gait changing through this region. At a scale factor of less than 0.03, Π_0 is near zero. With the naive method, the robot performance is not constant or intuitive throughout the change in size.

Using the nondimensional scaling method, the robot output Π_0 remains constant and predictable throughout the scaling, and the gait remains the same. The step size of the robot changes linearly with the lumen diameter. Using this method, the design variables need to adhere to the following trends to keep Π_1 through Π_{15} constant: length variables change linearly with the lumen diameter, density changes with d_e^{-2}, modulus of elasticity changes with d_e^{-1}, magnetization changes with $d_e^{-0.5}$, and lastly the dipole moment changes with $d_e^{2.5}$. The nondimensional scaling method results emphasize that the naive method is not a great way to drastically change the size of the robot; however, the nondimensional scaling trends would likely not be possible to strictly follow in practice. Nondimensional scaling trends would need to be used along with the design trends in Sec. 4.3 to adapt the robot to the constraints of a desired environment and application.

5 Discussion

The model developed in this paper uses a quasistatic approach to enable simulation of the robot and exploration of design parameters. An experimental setup was fabricated to validate the model. Two different environments were tested. In the polycarbonate tube, the robot's experimental velocity profile for four setup configurations is compared to the model simulation results. For all four configurations tested, the model simulation results of the velocity profiles are within one standard deviation of the mean experimental velocity during travel. On the *ex vivo* pig intestine, the model predictions follow the experimental results closely but are not as accurate as the rigid lumen. This is likely due to the unmodeled characteristic of the environment, such as biological irregularities and velocity-dependent friction. From these results, it is concluded that the model can be used to predict the soft robot's overall behavior and can be used to examine performance and design trends.

The first variable investigated is the alignment of the dipole moments in each foot of the robot. It was found that the best configuration of the dipole moments in the feet of the robot is a coaxial antiparallel configuration; whether the dipole moments both point inward or both point outward made no significant difference. The rest of the design variables' trends were explored. It was found that the speed of the robot generally increases when changing parameters that: (1) increase robot deformation under fixed forces and torques, (2) increase the magnitude of the magnetic forces and torques imposed on the robot, (3) decrease the resistance to motion, or (4) increase the step size for a given foot rotation.

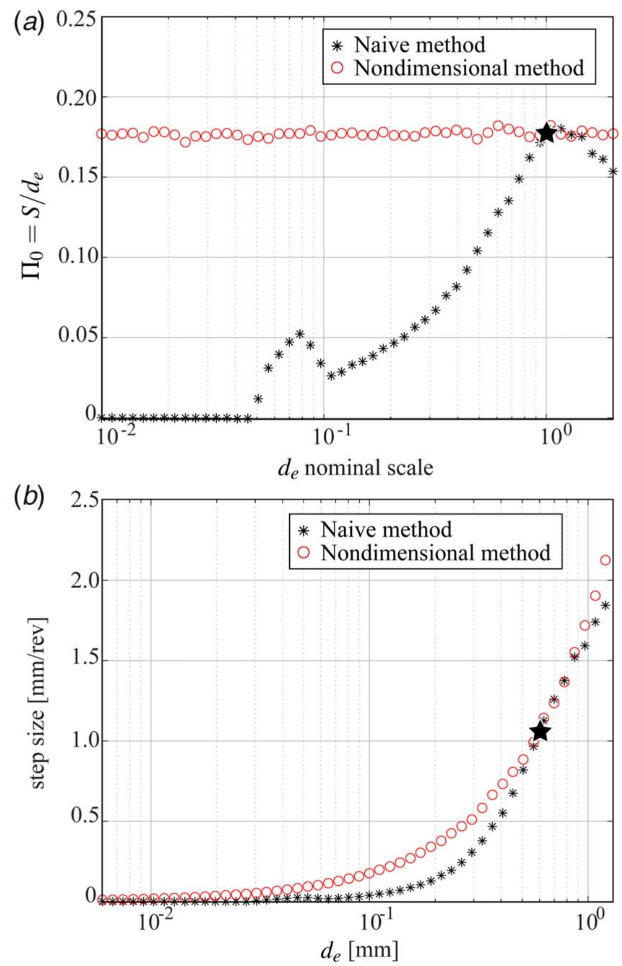

Fig. 9 Comparison of two scaling methods to scale the soft robot for different lumen environment diameters d_e: (1) scaling the robot length dimensions linearly with d_e (naive method) and (2) scaling the system by keeping all the nondimensional Π's in Table 1 constant (nondimensional method). (*a*) Scale of d_e from the nominal design compared to the dimensionless output parameter Π_0. (*b*) The lumen diameter compared to step size for the two methods. The black star marks the nominal design used in Figs. 7 and 8 and Table 1.

Using these design trends will aid in the future development of the endoluminal robot.

Lastly, scaling the robot size to work in various environmental lumen diameter scales was investigated using the model. Two methods were described. The first, the naive method, scaled the robot length dimensions linearly with the desired environmental lumen diameter. This method produced a functioning robot at scales of 0.03–2 times the nominal robot size but yielded results that would be hard to predict a priori. The second method scaled the robotic system (robot properties and actuator properties) based on desired environmental lumen diameter by keeping the independent nondimensional Π groups and other repeating variables constant. This method produced a very predictable result; the nondimensional step size stayed relatively constant throughout scaling. Changing the system's properties by keeping the Π groups constant is possible in the model; however, strictly following these trends in physical applications may not be practical. For example, to keep a constant Π_{11} as d_e is changed, the magnetization of the embedded magnets in the robot would need to change at a rate of $d_e^{-0.5}$. A magnet's magnetization can often not increase as the highest grade of a magnet is already used. Scaling with the nondimensional method may not always be physically possible, but it gives a good starting point for a design. When designing a robot for a specific lumen environment, the design trends and nondimensional scaling trends will give insight into how to achieve the desired output in a chosen environment. If scaling a particular robot to a specific environment and a nondimensional scaling trend cannot be satisfied, another parameter may be adjusted to offset the effects (using guidance from the design trends). For example, if the robot needed to be scaled to the desired lumen but the material of the robot, and therefore the modulus of elasticity, could not change, it may be possible to achieve the desired stiffness in the body of the robot by altering the body diameter. This change would, of course, have other effects on the gait but may bring the robot closer to the desired performance.

6 Conclusion

This paper presented a detailed model and analysis of a magnetically actuated inchworm-like soft robot that can travel through a lumen environment. The model will help mature the recently proposed robot concept and enable a deeper understanding of crucial design variables and how they influence the gait. The model was experimentally validated with a comparison to physical experiments using a plastic lumen environment and an *ex vivo* pig intestine. The model was shown to capture the robot's behavior well as it travels through the environments. To explore and analyze the design trends and scaling, nondimensional terms were derived using the Buckingham Π theorem. Using these terms, extensive simulations were performed that enable an in-depth understanding of which variables were sensitive to change, and their effect on the gait. The main trend being the greater the deformation of the body, the faster the robot. The robot concept can potentially be utilized in various endoluminal procedures in the human body. In the future, the locomotion concept explored here may extend the reach of endoluminal procedures and aid in developing controllable endoluminal devices. Additionally, motivated by preliminary results for the integration of electroactive polymer actuation [29], an in-depth investigation will be performed to study further performance enhancements.

Acknowledgment

This work was supported by the National Science Foundation (Grant No. 1830958). The authors would like to thank Professor Xiang He at Beihang University for his advice and discussion about the soft robot model.

Conflict of Interest

There are no conflicts of interest.

Data Availability Statement

Data provided by a third party are listed in Acknowledgment.

References

[1] Zheng, L., Min, Z. O., Varun, N., Vu, D. T., Hongliang, R., Theodoros, K., and Haoyong, Y., 2016, "Design of a Novel Flexible Endoscope-Cardioscope," ASME J. Mech. Rob., **8**(5), p. 051014.

[2] Loeve, A., Breedveld, P., and Dankelman, J., 2010, "Scopes Too Flexible···and Too Stiff," IEEE Pulse, **1**(3), pp. 26–41.

[3] Song, Y., Guo, S., Yin, X., Zhang, L., Hirata, H., Ishihara, H., and Tamiya, T., 2018, "Performance Evaluation of a Robot-Assisted Catheter Operating System With Haptic Feedback," Biomed. Microdev., **20**(2), p. 50.

[4] Pham, L. N., Steiner, J. A., Leang, K. K., and Abbott, J. J., 2020, "Soft Endoluminal Robots Propelled by Rotating Magnetic Dipole Fields," IEEE Trans. Med. Robot., **2**(4), pp. 598–607.

[5] Ashwin, K. P., and Ghosal, A., 2019, "A Soft-Robotic End-Effector for Independently Actuating Endoscopic Catheters," ASME J. Mech. Rob., **11**(6), p. 061004.

[6] Thomas, T. L., Kalpathy Venkiteswaran, V., Ananthasuresh, G. K., and Misra, S., 2021, "Surgical Applications of Compliant Mechanisms: A Review," ASME J. Mech. Rob., **13**(2), p. 020801.

[7] Kim, B., Park, S., and Park, J.-O., 2009, "Microrobots for a Capsule Endoscope," Proceedings of the IEEE/ASME International Conference on Advanced Intelligent Mechatronics, Singapore, July 14–17, pp. 729–734.

[8] Moglia, A., Menciassi, A., Schurr, M. O., and Dario, P., 2007, "Wireless Capsule Endoscopy: From Diagnostic Devices to Multipurpose Robotic Systems," Biomed. Microdev., **9**(2), pp. 235–243.

[9] Pi, X., Lin, Y., Wei, K., Liu, H., Wang, G., Zheng, X., Wen, Z., and Li, D., 2010, "A Novel Micro-fabricated Thruster for Drug Release in Remote Controlled Capsule," Sens. Actuator A Phys., **159**(2), pp. 227–232.

[10] Kim, B., Park, S., Jee, C. Y., and Yoon, S.-J., 2005, "An Earthworm-Like Locomotive Mechanism for Capsule Endoscopes," Proceedings of the IEEE/RSJ International Conference on Intelligent Robots and Systems, Edmonton, AB, Canada, Aug. 2–6, pp. 2997–3002.

[11] Hosokawa, D., Ishikawa, T., Morikawa, H., Imai, Y., and Yamaguchi, T., 2009, "Development of a Biologically Inspired Locomotion System for a Capsule Endoscope," Int. J. Med. Robot., **5**(4), pp. 471–478.

[12] Jung, K., Koo, J. C., Lee, Y. K., and Choi, H. R., 2007, "Artificial Annelid Robot Driven by Soft Actuators," Bioinspir. Biomim., **2**(2), pp. S42–549.

[13] Wang, K., Yan, G., Ma, G., and Ye, D., 2009, "An Earthworm-Like Robotic Endoscope System for Human Intestine: Design, Analysis, and Experiment," Ann. Biomed. Eng., **37**(1), pp. 210–221.

[14] Valdastri, P., Webster, R. J., Quaglia, C., Quirini, M., Menciassi, A., and Dario, P., 2009, "A New Mechanism for Mesoscale Legged Locomotion in Compliant Tubular Environments," IEEE Trans. Robot., **25**(5), pp. 1047–1057.

[15] Kim, H. M., Yang, S., Kim, J., Park, S., Cho, J. H., Park, J. Y., Kim, T. S., Yoon, E. -S., Song, S. Y., and Bang, S., 2010, "Active Locomotion of a Paddling-Based Capsule Endoscope in an In Vitro and In Vivo Experiment (With Videos)," Gastrointest. Endosc., **72**(2), pp. 381–387.

[16] Nam, J., Jeon, S., Kim, S., and Jang, G., 2014, "Crawling Microrobot Actuated by a Magnetic Navigation System in Tubular Environments," Sens. Actuators A: Phys., **209**, pp. 100–106.

[17] Formosa, G. A., Prendergast, J. M., Edmundowicz, S. A., and Rentschler, M. E., 2020, "Novel Optimization-Based Design and Surgical Evaluation of a Treaded Robotic Capsule Colonoscope," IEEE Trans. Robot., **36**(2), pp. 545–552.

[18] Mahoney, A. W., and Abbott, J. J., 2014, "Generating Rotating Magnetic Fields With a Single Permanent Magnet for Propulsion of Untethered Magnetic Devices in a Lumen," IEEE Trans. Robot., **30**(2), pp. 411–420.

[19] Lee, J.-S., Kim, B., and Hong, Y.-S., 2009, "A Flexible Chain-Based Screw Propeller for Capsule Endoscopes," Int. J. Precis. Eng. Manuf., **10**(4), pp. 27–34.

[20] Chiba, A., Sendoh, M., Ishiyama, K., Arai, K. I., Kawano, H., Uchiyama, A., and Takizawa, H., 2007, "Magnetic Actuator for a Capsule Endoscope Navigation System," J. Magn., **12**(2), pp. 89–92.

[21] Carta, R., Sfakiotakis, M., Pateromichelakis, N., Thoné, J., Tsakiris, D. P., and Puers, R., 2011, "A Multi-Coil Inductive Powering System for an Endoscopic Capsule With Vibratory Actuation," Sens. Actuator A Phys., **172**(1), pp. 253–258.

[22] Simaan, N., Yasin, R. M., and Wang, L., 2018, "Medical Technologies and Challenges of Robot-Assisted Minimally Invasive Intervention and Diagnostics," Annu. Rev. Control Robot. Auton. Syst., **1**(1), pp. 465–490.

[23] Simi, M., Valdastri, P., Quaglia, C., Menciassi, A., and Dario, P., 2010, "Design, Fabrication, and Testing of a Capsule With Hybrid Locomotion for Gastrointestinal Tract Exploration," IEEE/ASME Trans. Mechatron., **15**(2), pp. 170–180.

[24] Liang, H., Guan, Y., Xiao, Z., Hu, C., and Liu, Z., 2011, "A Screw Propelling Capsule Robot," Proceedings of the IEEE International Conference on Information and Automation, Shenzhen, China, June 6–8, pp. 786–791.

[25] Xin, W., Yan, G., and Wang, W., 2010, "Study of a Wireless Power Transmission System for an Active Capsule Endoscope," Int. J. Med. Robot., **6**(1), pp. 113–122.

[26] Sitti, M., and Wiersma, D. S., 2020, "Pros and Cons: Magnetic Versus Optical Microrobots," Adv. Mater., **32**(20), p. 1906766.

[27] Xie, J., Bi, C., Cappelleri, D. J., and Chakraborty, N., 2021, "Dynamic Simulation-Guided Design of Tumbling Magnetic Microrobots," ASME J. Mech. Rob., **13**(4), p. 041005.

[28] Kim, Y., Yuk, H., Zhao, R., Chester, S. A., and Zhao, X., 2018, "Printing Ferromagnetic Domains for Untethered Fast-Transforming Soft Materials," Nature, **558**(7709), pp. 274–279.

[29] Steiner, J. A., Hussain, O. A., Pham, L. N., Abbott, J. J., and Leang, K. K., 2019, "Toward Magneto-Electroactive Endoluminal Soft (MEESo) Robots," Proceedings of the ASME Dynamic Systems and Control Conference, Park City, UT, Oct. 8–11, p. V003T20A002.

[30] Petruska, A. J., and Abbott, J. J., 2013, "Optimal Permanent-Magnet Geometries for Dipole Field Approximation," IEEE Trans. Magn., **49**(2), pp. 811–819.

[31] Abbott, J. J., Diller, E., and Petruska, A. J., 2020, "Magnetic Methods in Robotics," Annu. Rev. Control Robot. Auton. Syst., **3**, pp. 57–90.

[32] Buckingham, E., 1914, "On Physically Similar Systems; Illustrations of the Use of Dimensional Equations," Phys. Rev., **4**(4), pp. 345–376.